



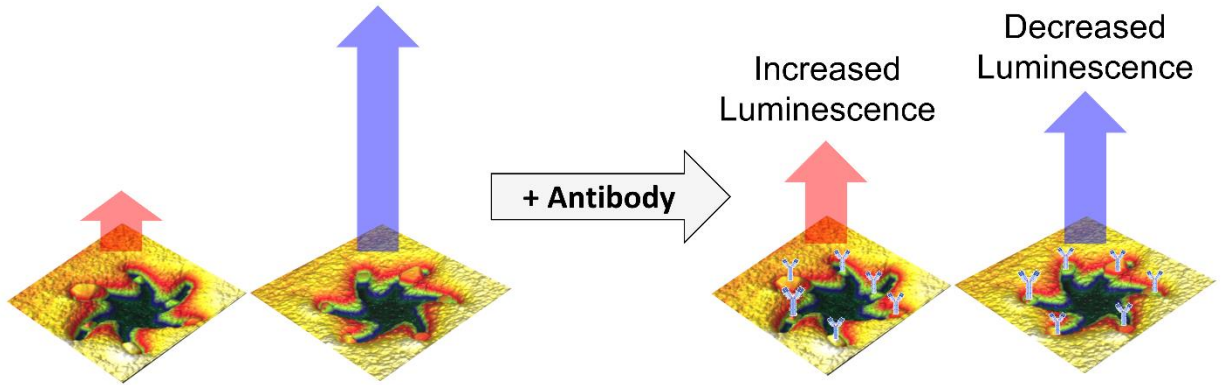
Hajji, M. et al. (2021) A chiral quantum metamaterial for hypersensitive biomolecule detection. *ACS Nano*, 15(12), pp. 19905-19916.

There may be differences between this version and the published version. You are advised to consult the publisher's version if you wish to cite from it.

<https://eprints.gla.ac.uk/259415/>

Deposited on: 24 November 2021

Enlighten – Research publications by members of the University of Glasgow
<https://eprints.gla.ac.uk>



A Chiral Quantum Metamaterial for Hypersensitive Biomolecule Detection.

Maryam Hajji¹, Michele Cariello¹, Cameron Gilroy¹, Martin Kartau¹, Christopher D. Syme¹, Affar Karimullah¹, Nikolaj Gadegaard², Aurélie Malfait³, Patrice Woisel³, Graeme Cooke¹, William J. Peveler¹ and Malcolm Kadodwala^{1}*

¹ School of Chemistry, University of Glasgow, Glasgow, G12 8QQ, UK

² School of Engineering, Rankine Building, University of Glasgow, Glasgow G12 8LT, U.K

³Univ. Lille, CNRS, INRAE, Centrale Lille, UMR 8207 - UMET - Unité Matériaux et Transformations, F-59000 Lille, France

ABSTRACT.

Chiral biological and pharmaceutical molecules are analysed with phenomena which monitor their very weak differential interaction with circularly polarised light. This inherent weakness results in detection levels for chiral molecules which is inferior, by at least 6 orders of magnitude, to the single molecule level achieved by state-of-the-art chirally insensitive spectroscopic measurements. Here we show a phenomenon based on chiral quantum metamaterials (CQM) which overcomes these intrinsic limits. Specifically, the emission from a quantum emitter, a semiconductor quantum dot (QD), selectively placed in a chiral nanocavity is strongly perturbed when individual biomolecules (here antibodies) are introduced into the cavity. The effect is extremely sensitive, with 6 molecules per nanocavity being easily detected. The phenomenon is attributed to the CQM being responsive to significant local changes in the optical density of states caused by the introduction of the biomolecule into the cavity. These local changes in the metamaterial electromagnetic environment, and hence the biomolecules, are invisible to “classical” light

scattering based measurements. Given the extremely large effects reported, our work presages next generation technologies for rapid hypersensitive measurements with applications in nanometrology and bio-detection.

KEYWORDS superchirality, quantum dots, quantum metamaterials, chiral, plasmonics.

Introduction

Spectroscopic methods, based on the differential absorption / scattering of circularly polarised light (CPL) by chiral media, are routinely used for rapid characterisation and detection of the structure of biomaterials.^{1, 2} The sensitivity of conventional chiroptical techniques, such as electronic or vibrational circular dichroism (CD / VCD), are inherently limited by the significant mismatch between the chiral length scales of CPL, equivalent to the wavelengths (for proteins typically 160-260 nm for CD and 5882 - 6667 nm for VCD), and that of molecules (size range 1-10 nm). Consequently, the stereostructural discrimination capabilities of chiroptical methods cannot be exploited in applications, such as biosensing, which require ultra-sensitivity. Chiroptical measurements can be enhanced using nanostructures to create near fields with enhanced intensity³⁻⁷ and / or enhanced chiral asymmetry.⁸⁻¹⁸ Such near field enhanced chiroptical techniques still rely on monitoring very weak dichroic signals, but monolayer sensitivities (~femtomole) are achieved. However, even this level of sensitivity pales when compared to the zeptomole (~1000 molecules)- single molecule / particle detection ranges that can be achieved using techniques based on labelling with bright, highly fluorescent species such as semiconductor quantum dots (QD).¹⁹ In general fluorescent-based techniques are not structurally incisive, requiring the synthesis of target molecules labelled with two chromophores in specific positions.²⁰ Consequently, if the detection sensitivity of QDs can be combined with the general structural incisiveness of chiroptical spectroscopy, one has the potential to probe the static and dynamic properties of biomaterials and interactions at \leq zeptomole level. This is a highly useful capability,

which for instance, could be exploited as a discrimination mechanism in next generations sensing and metrology technologies.

We report an intriguing phenomenon which enables chiral detection at the \leq zeptomole level. The concept, **Figure 1**, relies on chiral quantum metamaterials (CQM), QD placed into a chiral nanocavity. Using a bio-immobilisation strategy the QD can be deposited with high spatial selectivity within the chiral nano-cavity. Luminescence from the QD is sensitive to changes in local optical density of states of the electromagnetic (EM) environment of a chiral nano-resonator caused by binding of biomolecules. Chiral detection is based on monitoring very large changes in the intense QD emission, which are clearly visible by eye in the emission spectra. Specifically, zeptomole detection is achieved with both a large change in absolute spectral intensity, and a significant modification in spectral line shape. The large effects reported in this study have a dual impact, they simplify experimental measurements, facilitating potential applications, and enable high effective detection limits.

Results / Discussion

Chiral Quantum Metamaterial (CQM).

Metamaterials are engineered structures the properties of which are governed to a great extent by the geometric arrangement of the constituent components. Incorporating an element, such as a QD, creates a material, referred to as a quantum metamaterial, the properties of which can only be described by a combination of Maxwell's equations and quantum mechanics.²¹ For a QD which is weakly coupled to a nanocavity, emission is dependent on the optical local density of states, and can be understood within the framework of the Purcell effect.²² This is the enhancement of the spontaneous emission from a quantum emitter when placed within a resonant cavity. In a quantum

electrodynamics description, the Purcell effect arises from the modification, relative to free space, of the local optical density of states of the optical field due to the cavity environment.²³

Optical and AFM characterisation of CQM substrates

The CQM used in this study are based on plasmonic Au metafilms consisting of a square periodic lattice, of periodicity 700 nm, of six-armed cavities, **Figure 2 A**, subsequently referred to as shurikens, which are either left (LH) or right-handed (RH).²⁴ When immersed in aqueous environments both plasmonic metafilm enantiomorphs display a resonance feature spanning 1.569 – 1.797 eV, **Figure 3 A,B**, with a region of enhanced reflectivity at ~ 1.708 eV.²⁵ LH and RH Au metafilms are functionalised first with a biotinylated thiol-polymer (~5 nm thickness), that allows the specific binding of QDs through the strong biotin-streptavidin interaction, and then with a commercially produced semiconductor QD (QdotTM 705, Thermofisher) which are conjugated to 5 – 10 streptavidin protein units, **Figure 2 B**. No detectable electronic circular dichroism is observed over the range in which the QD has optical absorption. Thus, it can be inferred that the presence of the conjugated proteins does not significantly chirally perturb the electronic structure of the QD. The resonant region of the metafilms overlaps the emission from the QD ($\lambda_{\text{max}} = 705$ nm (1.759 eV)).

The polymer layer reduces the QD interaction with the Au film, indeed the lifetime of QD is not significantly reduced by immobilisation (confirmed by lifetime measurements). The QD display a high level of spatial selectivity for binding to the arm regions, close to the tips, of the shuriken indentation, **Figure 2 C and D**. The level of spatial selectivity of the QDs is demonstrated by AFM images from ensembles of LH and RH shuriken structures, **Figure 2 C**. In **figure 2D**, higher resolution 3-D AFM images of QDs immobilised to LH and RH enantiomorphs are shown. We

propose that this spatial selectivity arises because it maximises the contact of the QD with the polymer surfaces, providing a thermodynamic driver by maximising the level of biotin-streptavidin binding. On average over the whole of the surface, each arm of a shuriken has a bound QD within it; there are relatively few QD which are bound on the Au film between the nanostructures. It should be noted that the immobilisation of the QDs causes a small red shift (~ 2 meV) of the plasmonic resonance of the metafilms. This is consistent with the low coverage, ~ 6 QD per shuriken, produced by the immobilisation procedure. The CQM are subsequently used to detect an antibody, a monoclonal mouse IgG, which has been produced against streptavidin, henceforth referred to as anti-strept. The antibody will bind to the streptavidin surrounding the QD, which is not already attached to the biotin head group of the polymer. Given the approximate size of IgG, ~ 14 nm, combined with the steric constraints placed on the QD within the arm, it is proposed that ~ 1 antibody binds to each QD. Consequently, on average each shuriken will bind 6 IgG molecules, which is ~ 900 zeptomole over the whole $500 \times 500 \mu\text{m}$ array. Thus, within the field of view of the microscope this corresponds to the detection of 600 zeptomole. Optical rotatory dispersion (ORD) and reflectance spectra from the un-complexed and complexed CQM, show no significant differences, **Figure 3A-C**. Thus, demonstrating the insensitivity of light scattering measurements to the presence of zeptomole quantities of the biomolecules.

Luminescence spectra of un-complexed and complexed CQM

All luminescence spectra were excited with linearly polarised light, with detection at linearly polarisations which were either parallel or orthogonal to that of the excitation beam. Spectra were collected from the LH and RH CQM and for reference purposes data was also obtained from

adjacent areas of unstructured Au surface functionalised with QDs. Spectra were collected prior to, and then immediately after, complexation with anti-strept.

Spectra from un-complexed and complexed CQM are shown in **Figure 4** and **5**, while equivalents reference data from unstructured Au are shown in **Figure 6**. From an initial qualitative assessment of luminescence spectra there are some obvious patterns. The intensity of the emission from the CQM is much greater than that observed from QD immobilised on to the unstructured Au surface. The most important pattern in the data is a clear asymmetry between emission from LH and RH CQM. There is significantly more emission from RH enantiomorph compared to the LH, and there are differences in line shapes. The level of asymmetry, in terms of both intensity and line shape decreases after complexation with anti-strept. Finally, the similar levels of emission detected for the parallel and orthogonal detection geometries indicate that there is a high level of depolarisation of the emitted light. This observation can be understood in terms of the relative timescales of emission and (rotational) motion of the immobilised QD. As with all biological interactions the biotin-streptavidin bond will be a dynamic process, with it constantly breaking and reforming, thus allowing for the effective (rotational) motion of the QD. This random motion will occur on a time scale which is relatively close to the μs lifetimes of the emission of the QD. This will effectively smear out the linear polarisation of the incident excitation. Such depolarisation effects in emission from tumbling molecules in solution are well established.²⁶ However, the level of circular polarisation from such a rotating emitter will not be impacted.

To provide a foundation for quantitative analysis the luminescence spectra have been processed in two distinct ways. Firstly, the total emission intensities from the spectra are used to derive a series of parameters. The depolarisation ratio (ρ)

$$\rho = \frac{I_{Ortho}^K}{I_{Para}^K} \quad (1),$$

Where K is LH or RH CQM, or the unstructured Au, and I_{Ortho}^K and I_{Para}^K are the total intensities of the emission in the parallel and orthogonal detection direction for references. From these intensities an asymmetry parameter A can also derived,

$$A = \frac{I_{Para}^{RH}(Ortho)}{I_{Para}^{LH}(Ortho)} \quad (2)$$

Finally, an enhancement factor (F),

$$F = \frac{I_{Para}^{LH(RH)}(Ortho)}{I_{Para}^{Au}(Ortho)} \quad (3)$$

which parameterises the increase in the level of emission from the CQM relative to the unstructured surface. Values of ρ , A and F derived from un-complexed and complexed substrates are given in Tables 1-3.

The parameters ρ , A and F display significant enantiomorphous dependencies which are modified on complexation with anti-strept. For the unstructured Au surface there is no significant change in ρ after complexation. However, this is not the case for the CQM, where there is a significant decrease (increase) in the ρ value for LH (RH) enantiomorphs after complexation. A similar behaviour is observed for the F parameter, with complexation resulting in an increase (decrease) in the F parameter for the LH (RH) enantiomorph. These enantiomorphous dependent changes in the enhancement parameter led to a decrease in the asymmetry between LH and RH which is reflected in a decrease in the A parameter after complexation.

In addition to deriving parameters from the total emission intensities, changes in the peak shapes are quantified using fitting with Lorentzian and Gaussian components. Fits are shown with the corresponding experimental data in **Figure 4-6**. Within the precision of the fits the same three components, albeit with different relative intensities can be used for all the spectra. The mean positions of the three components derived from fitting all luminescence spectra (see Supplementary information), and subsequently labelled α , β and γ , are 1.677 ± 0.001 , 1.754 ± 0.002 and 1.807 ± 0.003 eV. The different relative contributions of the 3 components is the origin of the differing peak shapes between LH and RH enantiomorphs. For the un-complexed case, β and γ components are the dominant contributions in the LH and RH structures, respectively. On complexing the CQM with anti-strept the β component becomes the largest contribution to both LH and the RH substrates. It is this change in the relative contribution of the β component that results in the modification in line shape of the emission from LH CQM on complexation with anti-strept (**Figure 4-5**).

Luminescence of achiral QD references

For comparison, identical QD, which have not been conjugated to streptavidin and instead feature surface carboxylic acids, have been immobilised on to the metafilms using a chemical strategy (amide bond formation) which does not involve chiral molecules. Given the absence of any chiral molecular element these substrates will be subsequently referred to as “achiral QD references”. It should be noted that there are significant differences in the position of the achiral QD, compared to that produced by the streptavidin-biotin strategy. The achiral QD is located much closer, ~ 1 nm above, the Au surface. Crucially, the achiral QD immobilisation strategy is non spatially selective, as evidenced by AFM images. Based on the relative sizes of the luminescence from the

unstructured Au surfaces the carbodiimide mediated amide formation strategy that immobilises the achiral QDs produces surface coverages of $\sim 1/3$ of that of the biotin-streptavidin approach. Luminescence spectra taken from LH and RH achiral QD reference substrates, with one from an unstructured area of Au for comparison, are shown in **Figure 7**. Values of ρ , A and F , derived from these spectra are shown in Tables 1-3. There are substantial differences between the luminescence behaviours of the achiral QD and that of the CQMs. Principally, there are no significant asymmetries in the line shapes or intensities of the luminescence peak between LH and RH structures. All the spectra are fitted with single Gaussian peaks with similar widths, which are in turn not significantly different to those used to fit the streptavidin QD on unstructured Au. In addition to the lack of asymmetry, the achiral reference substrates, including QDs on the unstructured Au, have no detectable emission in the orthogonal polarisation direction, implying a $\rho \approx 0$. The absence of significant depolarisation of the emitted light can be attributed to a significant reduction in lifetime due to an increase in non-radiative decay, caused by the QD being located closer to the Au surface.²⁷ Absence of depolarisation implies that the lifetimes are now significantly shorter than the timescale of random motion of the QD.

Finally, the enhancement factor F is significantly reduced for the achiral QD, which we attribute to the non-spatially selective nature of the immobilisation strategy, producing a homogeneous random distribution of achiral QD across the metafilm.

Immobilisation using variations of the biotin-streptavidin strategy

The data from the achiral QD indicates the asymmetries in the luminescence data from the CQM is associated with the presence of the chiral protein layers. However, for completeness the possibility should be considered that the asymmetries in luminescence are derived from a non-

chiral effect. Specifically, there is the possibility that they are caused by streptavidin-biotin based functionalisation strategy (*i.e.* more QD being immobilised on the LH than the RH shurikens). It should be pointed out, that this is not consistent with the AFM data which shows no evidence for significant differences in QD densities on LH and RH enantiomorphs. Also, disparities in QD density cannot account for the difference in line shape between LH and RH un-complexed CQM, and the effects of complexation, in particular the increase in the emission intensity from the LH substrate, with anti-strept. To further support the hypothesis that the asymmetries arise from the presence of the chiral proteins we have prepared substrates with two modified streptavidin-biotin immobilisation strategies that produce surface densities which are significantly higher (~ 10 xs) and lower (≤ 0.1 xs) than the standard procedure (see Supplementary Information). Both substrates display the same RH / LH asymmetry in intensity. Luminescence spectra from the substrates with higher QD density are qualitatively like those obtained from the un-complexed substrate. The lower coverage QD was obtained by coadsorption of QD with free streptavidin. Thus, the nanocavities contain proportionately more chiral molecules to QDs than either the high density or standard substrate. The luminescence data obtained from the low-density substrate are qualitatively similar to that from the complexed substrate. Supporting the observation that an increase in the amount of chiral material in the nanocavity decreases the RH / LH asymmetry.

Purcell *versus* Chiral Purcell Effect

The data presented provides clear evidence that emissions from the CQM are sensitive to the presence of chiral materials. The biomaterials cause an asymmetry, in terms of both intensity and line shape, in emission from LH and RH CQM. Counter intuitively the experimental data shows that the asymmetry decreases as the amount of chiral material increases. To rationalise the

experimental observations, we now develop a discussion within a framework of the Purcell / chiral Purcell effect. This allows the luminescence data to be correlated to the properties of the electromagnetic (EM) environment.

When considered within a quantum electrodynamic framework, and with the application of Fermi's Golden Rule, spontaneous emission from excited states is dependent on the surrounding EM environment. Enhanced spontaneous emission can be engineered by increasing the optical density of states relative to that of the vacuum. For instance, by placing an emitter in a cavity with a resonant mode, spontaneous emission is enhanced, a phenomenon known as the Purcell effect.²² Alternatively, in the absence of a cavity, large densities of optical states generated in the vicinity of metallic nanostructures also cause enhanced emission.²⁸ In both cases the enhanced emission rates can be rationalised with a Purcell formalism. Where the enhancement in emission rate, called the Purcell factor (F_P), is

$$F_P = \frac{3}{4\pi^2} \left(\frac{\lambda_0}{n}\right)^3 \left(\frac{Q}{V_P}\right) \quad (4)$$

where Q is the mode's quality factor, n the refractive index of the medium, λ_0 is the resonance wavelength, and V_P is the effective mode volume,

$$V_P = \frac{U}{2u_{E,max}} \quad (5)$$

where U is the total energy and $u_{E,max}$ is the energy density. Q and $1/V$ can be considered to be the spectral and spatial energy density respectively of the resonant mode.²⁸

The Purcell formalism has been extended to chiral light matter interactions in optical resonators, where excited states are coupled to chiral optical states.²⁹ The critical parameter in this framework

is the optical chirality density (C), which is equivalent to optical spin density. The C of an EM field^{13, 30-32} is defined as,

$$C = \frac{1}{2}(\mathbf{D} \cdot \dot{\mathbf{B}} - \mathbf{B} \cdot \dot{\mathbf{D}}), \quad (6)$$

where \mathbf{D} is the displacement field, \mathbf{B} the magnetic induction and $\dot{\mathbf{D}}$ and $\dot{\mathbf{B}}$ are their respective time-derivatives. C can be used to parameterise the chiral asymmetry of EM fields.¹² C is a conserved quantity,³⁰ like energy, and has been used in continuity expressions for the chiral (optical spin) properties of light derived from Maxwell's equations.³³ The C of EM fields is a crucial parameter in understanding the chiral Purcell effect, since the enhancement it gives rise to, originates from an increase in the optical chirality density (spin density) in a chiral resonator relative to free space. A chiral Purcell factor (F_C) that quantifies the enhancement of emission in a chiral system can be defined as,

$$F_C = \frac{1}{4\pi^2} \left(\frac{\lambda_0}{n}\right)^3 \left(\frac{Q}{V_C}\right) \quad (7)$$

where V_c is the chiral mode volume and represents the spatial confinement of chirality (or optical spin) of light, and $1/V_c$ reflects the chiral energy density. V_C is defined as

$$V_C = \frac{U}{u_{C,max}} = -\frac{\omega U}{cC_{max}} \quad (8)$$

where U and $u_{C,max}$ are the total energy and maximum chiral energy density respectively. $u_{C,max} = -cC_{max}/\omega$ where C_{max} is the maximum optical chirality density.

The experimentally observed asymmetry in the enhanced emission from enantiomorphs of the CQM can potentially originate from either the Purcell or chiral Purcell effects. This is because the

presence of the chiral biomolecules in both the un-complexed and complexed CQM locally alter both $|E|$ and C . Consequently, given that from **Figures 3A** and **B** it is clear that complexation with anti-strept has a negligible effect on the Q of the resonances, modifications in the emission must be due to changes in either V_P or V_c .

Numerical EM simulations

Numerical (finite element method) EM simulations have been performed to elucidate whether the Purcell or chiral Purcell effect is responsible for the asymmetric luminescence behaviour from un-complexed / complexed CQM. The simulations are based on an idealised version of the real CQM structures shown in **Figure 2C**. Although, in the real structure the QDs adopt a range of positions within the arms of the shurikens, for simplicity in the idealised model we have located them at the ends of the arms. In the model the QD is represented by a spherical achiral dielectric core (diameter 10 nm), which is surrounded by a chiral dielectric layer (thickness 5 nm) which represents the conjugated proteins. To replicate the complexed CQM an additional hemispherical chiral dielectric layer of 5 nm thickness is included, **Figure 8A**. How chiral dielectric properties are accounted for in numerical simulations of chiral plasmonic systems has been described previously.^{11, 25, 34-36} The chiral response of the dielectric layer is parameterised by a second rank tensor ξ . For an isotropic layer $\xi_{xx} = \xi_{yy} = \xi_{zz}$, with all elements being zero if optical activity as an electric dipole – magnetic dipole (E_1M_1) origin.^{11, 25, 37} In the current simulations a $|\xi| = 5 \times 10^{-4}$, which is comparable to values used previously to mimic protein layers.³⁷ Reflectance spectra, **Figure 8B, C**, derived from simulations based on the idealised model are in good agreement with the experimental data, **Figure 3**, which provides validation of the robustness of the methodology.

Using the data provided by the simulations, values of V_P and V_C truncated to the protein layers, can be calculated for LH and RH enantiomorphs of the un-complexed / complexed CQM over the emission energy range, **Figure 9A, B**. By using these values in Equations 4 and 7, with other parameters either derived from experimental data or estimated from the literature, F_P and F_C can be calculated. For simplicity the chiral asymmetry of n , typically $\leq 10^{-3}$, has been neglected. Subsequently, by multiplying F_P and F_C with the Gaussian function used to fit the non-enhanced emission from the QDs on the unstructured Au surface, simulated emission spectra can be generated, **Figure 10A, B**. It is immediately apparent that only V_C , and the spectra derived from it, show significant asymmetries, in terms of both line shape and intensity, between enantiomorphs. In addition, only the spectra derived from the chiral Purcell effect display a change on complexation. However, there are clear inconsistencies between the modelled and experimental spectra. The line shapes of the modelled spectra are in poor agreement with experimental data. However, the simulations do have three discernible peaks, consistent with the experimental data. Also, although the simulations replicate the reduction in the intensity of signal from the RH enantiomorph on complexation, they do not show the concurrent increase in the LH. We propose that these discrepancies can be rationalised with the consideration of two factors. Firstly, the simple idealised model used in the simulations does not adequately replicate the structure of the “real” CQM. Specifically, the heterogeneity of the location of the QD within the shuriken structure, in terms of both lateral and vertical position, are not accounted for in the model. Also, the model accounts neither for the variability of QD morphology and size, nor the level of streptavidin conjugation. Secondly, within the precision of the models, spectra derived from V_C and V_P are of comparable magnitude. Consequently, the experimentally observed spectra could be a combination of both Purcell and chiral Purcell responses. Indeed, the contribution that each

makes to the overall emission may be modified by complexation. This hypothesis is supported when one considers the behaviour of the complexed CQM. It would be expected that the complexed CQM would have a greater relative contribution from the Purcell effect than the uncomplexed case, as V_C increases, and V_P does not alter significantly for both enantiomorphs on complexation. This is consistent with both the line shape for the complexed case, which shows a level of similarity with that predicted by the Purcell model, and the reduction in the level of asymmetry between LH and RH enantiomorphs.

Despite the caveats outlined above, the numerical simulations do clearly demonstrate that only the contributions from the chiral Purcell effect can give rise to significant asymmetries in the luminescence behaviour when the chiral environments surrounding the QD is modified. Consequently, allowing spectroscopic detection of chiral (bio)molecules at the \leq zeptomole level.

Conclusions

The combined experimental and numerical simulated data presented demonstrate that luminescence from QDs placed spatially selectively within a chiral nanocavity can detect the presence of chiral (bio)molecules at the \leq zeptomole level. The phenomena can be understood within the framework of the chiral Purcell effect. Specifically, QD luminescence is an extremely sensitive probe of changes in the spatial confinement of local helicity caused by the modification of C induced by the introduction of single biomolecules into a region of space.

In the broadest sense, this work breaks the link between chiral spectroscopy and the measurement of very weak dichroic effects. It demonstrates the superior capabilities of techniques based on the measurement of local near, rather than far field properties for chiral sensing. Far field (chir)optical responses of nanostructures are correlated to the global EM near field environment. Consequently,

molecules cannot be detected if they have concentrations too low to cause significant changes to the global EM environment. For instance, in this study the presence of antibodies did not cause detectable changes to either reflectance or chirally sensitive optical rotatory dispersion spectra measured in the far field. However, the introduction of even small amounts of material can result in significant local perturbations, even though these only result in a small net change in the global EM environment. Using CQM, where QD act as reporters of the EM environment, allow the large local changes to be detected. In the exemplar systems studied here this enabled the detection of ~ 6 antibody molecules per nanostructure. Although, for completeness data for both LH and RH structures were measured here, detection can be achieved by using just a single enantiomorph of a metamaterial. This contrast to the case for the isolated QD, the emission intensity from which is insensitive to the binding of the antibody. Consequently, with appropriate experimental design and instrumentation which would allow measurements on a single nanostructure, the effect would enable the detection and characterisation approaching single molecule detection. In this study the spatially selective placement of the QDs, relied on the streptavidin – biotin interaction, which limits potential targets for detection. If a more generic spatially selective immobilisation strategy was used, such as one based on nano-localised heating,³⁸ the necessity of using QD conjugated to proteins would be removed. This would enable a wide range of chiral materials to be detected. Additionally, for extra flexibility the QDs could be substituted with an appropriate dye molecule if necessary. This study presages next generation nanometrology technologies for chiral detection with enhanced sensitivities, with applications in molecular diagnostics and nanometrology.

Methods / Experimental

Sample nanofabrication

The shuriken structure was fabricated on the Polycarbonate substrate using an injection moulding machine (ENGEL) was described in detail elsewhere.³⁹ The pattern defined on the substrate had a depth of ~80nm and a length of 500nm from arm to arm. After fabrication, the slide was cleaned with IPA and dried with N₂ gas. The cleaned slide was metal evaporated using Plassys MEB-400s to the thickness of 100nm Au and then cleaned in an oxygen plasma asher.

Biotin-Streptavidin Functionalisation

A biotinylated thiol polymer (NIPAM) was synthesised as described below and diluted into PBS buffer (10x, pH 7.4) with the factor of 10:1 (PBS: Polymer) concentration. The substrate was left in 300 μ L of NIPAM solution for 24 hours to allow to produce a self-assembled monolayer (SAM) on Au surface. The sample was rinsed with PBS and the optical rotatory dispersion (ORD) spectra and reflectivity were collected from LH and RH samples while immersed in both water and PBS. QdotTM 705 Streptavidin Conjugate (Thermofisher) were deposited on sample and left for two hours, followed by rinsing in 0.1% NaOH/Tween (Sigma-Aldrich) which removes non-specifically bound / weakly bound streptavidin. After preparing the sample, measurements were taken in the Photoluminescent (PL) measurement microscope to collect luminescence spectra using a linear polarisation in water and PBS. The antibody solution was added to the sample for two hours and rinsed with 0.1% NaOH/Tween (Sigma-Aldrich) to obtain PL spectra. The high coverage QD structures were produced by not doing the Tween surfactant wash. The QD / Streptavidin co-adsorbed structures were produced by using a solution with a 10:1 ratio by molar concentration of streptavidin to QDs.

EDC-NHS functionalisation for achiral QD reference

The metafilms were treated with 50 mM Carboxy-PEG-Thiol CT(PEG)₁₂ (Thermo: 26133) and 50 mM Methyl-PEG-Thiol MT(PEG)₄ (Thermo: 26132) (1:1, v/v) for 18 hours. The samples were rinsed with deionised water and dried with nitrogen. Subsequently the samples were treated with 180 mM EDC (1-ethyl-3-(3-dimethylaminopropyl)carbodiimide hydrochloride) (Thermo: 22980) and 180 mM Sulfo-NHS (N-hydroxysulfosuccinimide) (Thermo: 25410) (1:1, v/v) for 15 minutes in MES (pH 6.0) buffer. Conjugation reagent solution was removed, the metafilms were rinsed with PBS (pH 7.4, Thermo: 10010023), and 800 nM solution of amine-terminated quantum dot (Qdot™ 705 ITK™ Amino (PEG) Quantum Dots) (solution applied for 60 minutes.)

Optical rotatory dispersion (ORD) and reflectivity measurements

A custom-made polarization microscope has been used to collect the linear optical measurement of our samples.²⁴ The set-up contains a tungsten halogen lamp (Thorlabs) Lightsource that propagates through a collimating lens, Glan-Thomson polariser (Thorlabs), 50:50 beamsplitter and a focused beam 10x objective lens (Olympus). The reflected beam propagates back from the second Glan-Thompson polarisers (Thorlabs) and captures by the spectrometer (Ocean Optics USB400). The sample was positioned and focused using a camera (Thorlabs DCC1645C) after the analyser. The Stokes methods are using to record the ORD spectra at four analyser angles (0°, ±45° and 90°) concerning the incident polarisation for both LH and RH pairs of samples.

Luminescence setup

Luminance measurement was carried out using a 404 nm laser diode with a 180-mA fixed current and maximum optical power output of ~17 mW measured using a digital power meter. The two (linear) polarisers at the input after the laser diode were mounted to adjust the input power. The first polarizer was used to modify the input power and the second polarized to define the input

polarization. The position of the sample and alignment of the laser on the desired point of the sample has been monitored using an optical camera. The luminance signals were captured using a CCD camera mounted on the top of the configuration. All components were rigidly mounted on an optical bench.

Numerical electromagnetic modelling

A commercial finite element package (COMSOL V5.6 Multiphysics software, Wave Optics module) has been used to simulate the intensity and chiral asymmetry of EM fields produced across the sample. Periodic boundary conditions have been imposed on the sides of the meta-film (*i.e.*, equivalent to simulating a meta-film array). Reflections were minimized using a perfectly matched layer (PML) above and below the input and output ports.

Linearly polarised EM waves were performed at normal incidence onto the meta-film. The finite-element method has been used to solve Maxwell's equations over a distinctive geometry which allows the optical chirality and E-field intensity to be measured in COMSOL. Additional 6 Quantum dots domains were placed on top of shuriken structure arms. The Quantum dots domains consist of a core structure surrounded with 5nm Protein shell were defined with a refractive index of 1.5.⁴⁰ The Protein domains were chiral with the optical chirality parameter of $|\xi| = 5 \times 10^{-4}$. Another 5nm shell has been added on top of the Protein shell as an antibody domain with the same refractive index of Protein. The optical chirality and E-field intensity of the protein layers were derived by integrating the geometrical model using the volume integration method

ASSOCIATED CONTENT

Supporting Information is available free of charge at

- A the optical set up of the luminescence spectrometer (Figure S1), the idealised model of the CQM used for numerical simulations (figure S2), spatial distribution of the C at a range of wavelength (figure S3), the parameters used in the fits of the luminescence data are tabulated, luminescence data from the two alternative QD deposition strategies, a description of the synthesis of the polymer used to create the SAM is given.

AUTHOR INFORMATION

Corresponding Author

*to whom correspondence should be addressed. Email: Malcolm.Kadodwala@glasgow.ac.uk

Author Contributions

The manuscript was written through contributions of all authors. All authors have given approval to the final version of the manuscript

Funding Sources

Any funds used to support the research of the manuscript should be placed here (per journal style).

.

ACKNOWLEDGMENT

The authors acknowledge financial support from the Engineering and Physical Sciences Research Council (EP/P00086X/1 and EP/M024423/1) Technical support from the James Watt Nanofabrication Centre (JWNC). CG's work was supported by the EPSRC CDT in Intelligent Sensing and Measurement, Grant Number EP/L016753/1. WJP acknowledges the University of Glasgow for an LKAS fellowship. MK acknowledges the Leverhulme Trust for the award of a Research Fellowship (RF-2019-02)

REFERENCES

- (1) Kelly, S. M.; Price, N. C. The Use of Circular Dichroism in the Investigation of Protein Structure and Function. *Current Protein & Peptide Science* **2000**, *1* (4), 349-384.
- (2) Blanch, E. W.; Barron, L. D. Raman Optical Activity of Biological Molecules. In *Emerging Raman Applications and Techniques in Biomedical and Pharmaceutical Fields*, Matousek, P., Morris, M. D. Eds.; Biological and Medical Physics Biomedical Engineering, Springer, New York 2010; 153-177.
- (3) J. Langer, D. J. de Aberasturi, J. Aizpurua, R. A. Alvarez-Puebla, B. Auguie, J. J. Baumberg, G. C. Bazan, S. E. J. Bell, A. Boisen, A. G. Brolo, J. Choo, D. Cialla-May, V. Deckert, L. Fabris, K. Faulds, F. J. G. de Abajo, R. Goodacre, D. Graham, A. J. Haes, C. L. Haynes, C. Huck, T. Itoh, M. Ka, J. Kneipp, N. A. Kotov, H. Kuang, E. C. Le Ru, H. K. Lee, J. F. Li, X. Y. Ling, S. A. Maier, T. Mayerhofer, M. Moskovits, K. Murakoshi, J. M. Nam, S. Nie, Y. Ozaki, I. Pastoriza-Santos, J. Perez-Juste, J. Popp, A. Pucci, S. Reich, B. Ren, G. C. Schatz, T. Shegai, S. Schlucker, L. L. Tay, K. G. Thomas, Z. Q. Tian, R. P. Van Duyne, T. Vo-Dinh, Y. Wang, K. A. Willets, C. Xu, H. Xu, Y. Xu, Y. S. Yamamoto, B. Zhao, L. M. Liz-Marzan. Present and Future of Surface-Enhanced Raman Scattering. *Acs Nano* **2020**, *14* (1), 28-117,
- (4) Adato, R.; Altug, H. *In-situ* Ultra-Sensitive Infrared Absorption Spectroscopy of Biomolecule Interactions in Real Time with Plasmonic Nanoantennas. *Nature Communications* **2013**, *4*, 10.
- (5) Pour, S. O.; Bell, S. E. J.; Blanch, E. W. Use of a Hydrogel Polymer for Reproducible Surface Enhanced Raman Optical Activity (SEROA). *Chemical Communications* **2011**, *47* (16), 4754-4756.

(6) Pour, S. O.; Rocks, L.; Faulds, K.; Graham, D.; Parchansky, V.; Bour, P.; Blanch, E. W. Through-Space Transfer of Chiral Information Mediated by a Plasmonic Nanomaterial. *Nature Chemistry* **2015**, *7* (7), 591-596.

(7) Lieberman, I.; Shemer, G.; Fried, T.; Kosower, E. M.; Markovich, G. Plasmon-Resonance-Enhanced Absorption and Circular Dichroism. *Angewandte Chemie-International Edition* **2008**, *47* (26), 4855-4857.

(8) Mun, J.; Kim, M.; Yang, Y.; Badloe, T.; Ni, J. C.; Chen, Y.; Qiu, C. W.; Rho, J. Electromagnetic Chirality: From Fundamentals to Nontraditional Chiroptical Phenomena. *Light-Science & Applications* **2020**, *9* (1), 18.

(9) Hendry, E.; Carpy, T.; Johnston, J.; Popland, M.; Mikhaylovskiy, R. V.; Laphorn, A. J.; Kelly, S. M.; Barron, L. D.; Gadegaard, N.; Kadodwala, M. Ultrasensitive Detection and Characterization of Biomolecules Using Superchiral Fields. *Nature Nanotechnology* **2010**, *5* (11), 783-787.

(10) Hendry, E.; Mikhaylovskiy, R. V.; Barron, L. D.; Kadodwala, M.; Davis, T. J. Chiral Electromagnetic Fields Generated by Arrays of Nanoslits. *Nano Letters* **2012**, *12* (7), 3640-3644.

(11) Garcia-Guirado, J.; Svedendahl, M.; Puigdollers, J.; Quidant, R. Enantiomer-Selective Molecular Sensing Using Racemic Nanoplasmonic Arrays. *Nano Letters* **2018**, *18* (10), 6279-6285.

(12) Garcia-Guirado, J.; Svedendahl, M.; Puigdollers, J.; Quidant, R. Enhanced Chiral Sensing with Dielectric Nanoresonators. *Nano Letters* **2020**, *20* (1), 585-591.

- (13) Zhao, Y.; Askarpour, A. N.; Sun, L.; Shi, J.; Li, X.; Alu, A. Chirality Detection of Enantiomers Using Twisted Optical Metamaterials. *Nature Communications* **2017**, *8*.
- (14) Xiao, T.-H.; Cheng, Z.; Luo, Z.; Isozaki, A.; Hiramatsu, K.; Itoh, T.; Nomura, M.; Iwamoto, S.; Goda, K. All-Dielectric Chiral-Field-Enhanced Raman Optical Activity. *Nature Communications* **2021**, *12* (1), 3062.
- (15) Solomon, M. L.; Abendroth, J. M.; Poulikakos, L. V.; Hu, J.; Dionne, J. A. Fluorescence-Detected Circular Dichroism of a Chiral Molecular Monolayer with Dielectric Metasurfaces. *Journal of the American Chemical Society* **2020**, *142* (43), 18304-18309.
- (16) Tullius, R.; Platt, G. W.; Khosravi Khorashad, L.; Gadegaard, N.; Laphorn, A. J.; Rotello, V. M.; Cooke, G.; Barron, L. D.; Govorov, A. O.; Karimullah, A. S.; Kadodwala, M. Superchiral Plasmonic Phase Sensitivity for Fingerprinting of Protein Interface Structure. *ACS Nano* **2017**, *11*, 12049-12056.
- (17) Tang, Y.; Cohen, A. E. Optical Chirality and Its Interaction with Matter. *Physical Review Letters* **2010**, *104* (16) 163901.
- (18) Tang, Y. Q.; Cohen, A. E. Enhanced Enantioselectivity in Excitation of Chiral Molecules by Superchiral Light. *Science* **2011**, *332* (6027), 333-336.
- (19) Michalet, X.; Pinaud, F. F.; Bentolila, L. A.; Tsay, J. M.; Doose, S.; Li, J. J.; Sundaresan, G.; Wu, A. M.; Gambhir, S. S.; Weiss, S. Quantum Dots for Live Cells, *in vivo* Imaging, and Diagnostics. *Science* **2005**, *307* (5709), 538-544.
- (20) Feng, X. A.; Poyton, M. F.; Ha, T. Multicolor Single-Molecule FRET for DNA and RNA Processes. *Current opinion in structural biology* **2021**, *70*, 26-33.

- (21) Solntsev, A. S.; Agarwal, G. S.; Kivshar, Y. Y. Metasurfaces for Quantum Photonics. *Nature Photonics* **2021**, *15* (5), 327-336.
- (22) Pound, R. V.; Purcell, E. M. Measurement of Magnetic Resonance Absorption by Nuclear Moments in a Solid. *Physical Review* **1946**, *69* (11-1), 681-681.
- (23) Xu, D.; Xiong, X.; Wu, L.; Ren, X. F.; Png, C. E.; Guo, G. C.; Gong, Q. H.; Xiao, Y. F. Quantum Plasmonics: New Opportunity in Fundamental and Applied Photonics. *Advances in Optics and Photonics* **2018**, *10* (4), 703-756.
- (24) Karimullah, A. S.; Jack, C.; Tullius, R.; Rotello, V. M.; Cooke, G.; Gadegaard, N.; Barron, L. D.; Kadodwala, M. Disposable Plasmonics: Plastic Templated Plasmonic Metamaterials with Tunable Chirality. *Advanced Materials* **2015**, *27* (37), 5610-5616.
- (25) Kelly, C.; Khorashad, L. K.; Gadegaard, N.; Barron, L. D.; Govorov, A. O.; Karimullah, A. S.; Kadodwala, M. Controlling Metamaterial Transparency with Superchiral Fields. *Acs Photonics* **2018**, *5* (2), 535-543.
- (26) Jameson, D. M.; Ross, J. A. Fluorescence Polarization/Anisotropy in Diagnostics and Imaging. *Chemical Reviews* **2010**, *110* (5), 2685-2708.
- (27) Waldeck, D. H.; Alivisatos, A. P.; Harris, C. B. Nonradiative Damping of Molecular Electronic Excited-States by Metal Surfaces. *Surface Science* **1985**, *158* (1-3), 103-125.
- (28) Maier, S. A. Plasmonic Field Enhancement and SERS in the Effective Mode Volume Picture. *Optics Express* **2006**, *14* (5), 1957-1964.
- (29) Yoo, S.; Park, Q. H. Chiral Light-Matter Interaction in Optical Resonators. *Physical Review Letters* **2015**, *114* (20), 203003.

(30) Lipkin, D. M. Existence of New Conservation Law in Electromagnetic Theory. *J Math Phys* **1964**, *5* (5), 696-700.

(31) Proskurin, I.; Ovchinnikov, A. S.; Nosov, P.; Kishine, J. Optical Chirality in Gyrotropic Media: Symmetry Approach. *New J Phys* **2017**, *19*, 063021.

(32) Bliokh, K. Y.; Nori, F. Characterizing Optical Chirality. *Phys Rev A* **2011**, *83* (2), 021803(R).

(33) Kelly, C.; MacLaren, D. A.; McKay, K.; McFarlane, A.; Karimullah, A. S.; Gadegaard, N.; Barron, L. D.; Franke-Arnold, S.; Crimin, F.; Goette, J. B.; Barnett, S. M.; Kadodwala, M. Controlling the Symmetry of Inorganic Ionic Nanofilms with Optical Chirality. *Nature Communications* **2020**, *11* (1)..

(34) Abdulrahman, N. A.; Fan, Z.; Tonooka, T.; Kelly, S. M.; Gadegaard, N.; Hendry, E.; Govorov, A. O.; Kadodwala, M. Induced Chirality through Electromagnetic Coupling between Chiral Molecular Layers and Plasmonic Nanostructures. *Nano Letters* **2012**, *12* (2), 977-983.

(35) Tullius, R.; Karimullah, A. S.; Rodier, M.; Fitzpatrick, B.; Gadegaard, N.; Barron, L. D.; Rotello, V. M.; Cooke, G.; Laphorn, A.; Kadodwala, M. "Superchiral" Spectroscopy: Detection of Protein Higher Order Hierarchical Structure with Chiral Plasmonic Nanostructures. *Journal of the American Chemical Society* **2015**, *137* (26), 8380-8383.

(36) Gilroy, C.; Hashiyada, S.; Endo, K.; Karimullah, A. S.; Barron, L. D.; Okamoto, H.; Togawa, Y.; Kadodwala, M. Roles of Superchirality and Interference in Chiral Plasmonic Biodetection. *Journal of Physical Chemistry C* **2019**, *123* (24), 15195-15203.

(37) Kelly, C.; Tullius, R.; Laphorn, A. J.; Gadegaard, N.; Cooke, G.; Barron, L. D.; Karimullah, A. S.; Rotello, V. M.; Kadodwala, M. Chiral Plasmonic Fields Probe Structural Order of Biointerfaces. *Journal of the American Chemical Society* **2018**, *140* (27), 8509-8517.

(38) Jack, C.; Karimullah, A. S.; Tullius, R.; Khorashad, L. K.; Rodier, M.; Fitzpatrick, B.; Barron, L. D.; Gadegaard, N.; Laphorn, A. J.; Rotello, V. M.; Cooke, G.; Govorov, A. O.; Kadodwala, M. Spatial Control of Chemical Processes on Nanostructures Through Nano-Localized Water Heating. *Nature Communications* **2016**, *7*. DOI: 10.1038/ncomms10946.

(39) Gadegaard, N.; Mosler, S.; Larsen, N. B. Biomimetic Polymer Nanostructures by Injection Molding. *Macromolecular Materials and Engineering* **2003**, *288* (1), 76-83.

(40) (25) Phan, H. T.; Bartelt-Hunt, S.; Rodenhausen, K. B.; Schubert, M.; Bartz, J. C. Investigation of Bovine Serum Albumin (BSA) Attachment onto Self-Assembled Monolayers (SAMs) Using Combinatorial Quartz Crystal Microbalance with Dissipation (QCM-D) and Spectroscopic Ellipsometry (SE). *PloS one* 2015, *10* (10), e0141282.

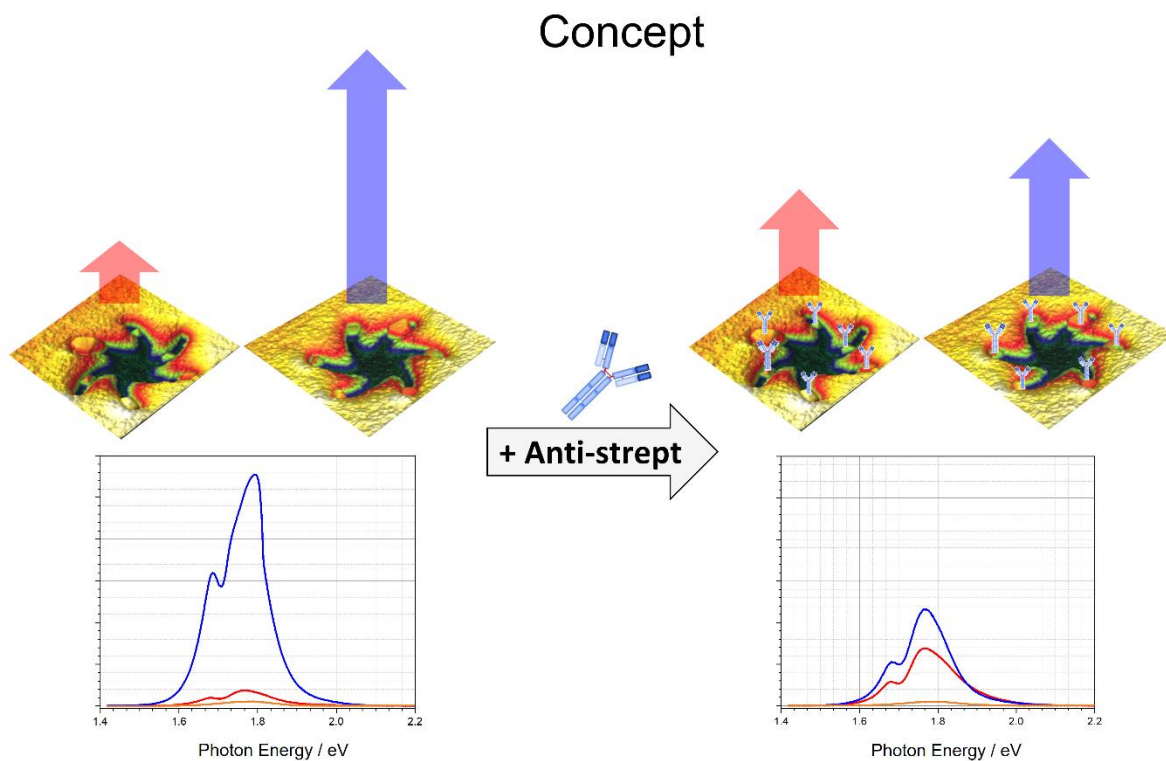


Figure 1. Graphical representation of the central concept of the current work. Luminescence from LH and RH CQM is highly sensitive to changes in optical helicity / chirality in local environment of the QD. This allows the introduction of ~ 6 biomolecules per nanostructure to be detected.

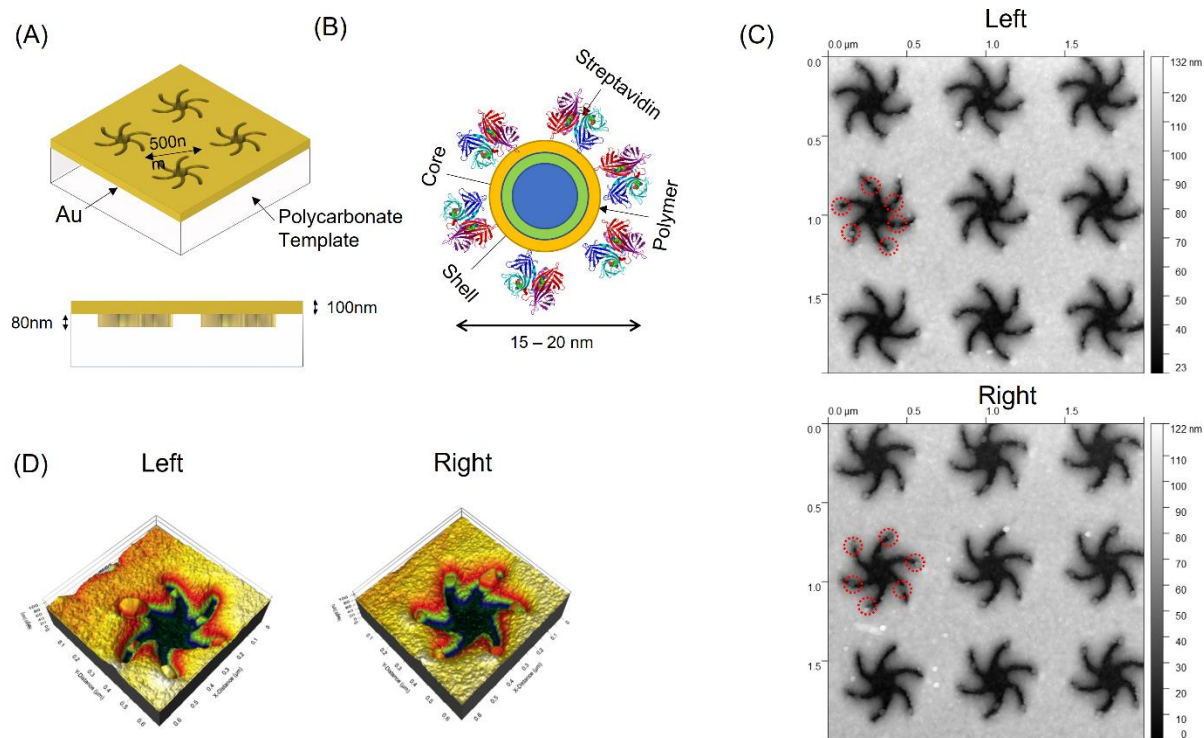


Figure 2. (A) The top and side views of the Au metafilms; (B) A graphic showing the structure of the QD; (C) AFM images of CQM (un-complexed), illustrating the spatially selective positioning of the QD for an area of 9 structures. To aid the eye some QD are highlighted with red circles; and (D) High resolution images of LH and RH CQM (complexed), which illustrate the distribution of sizes and morphologies of the QDs.

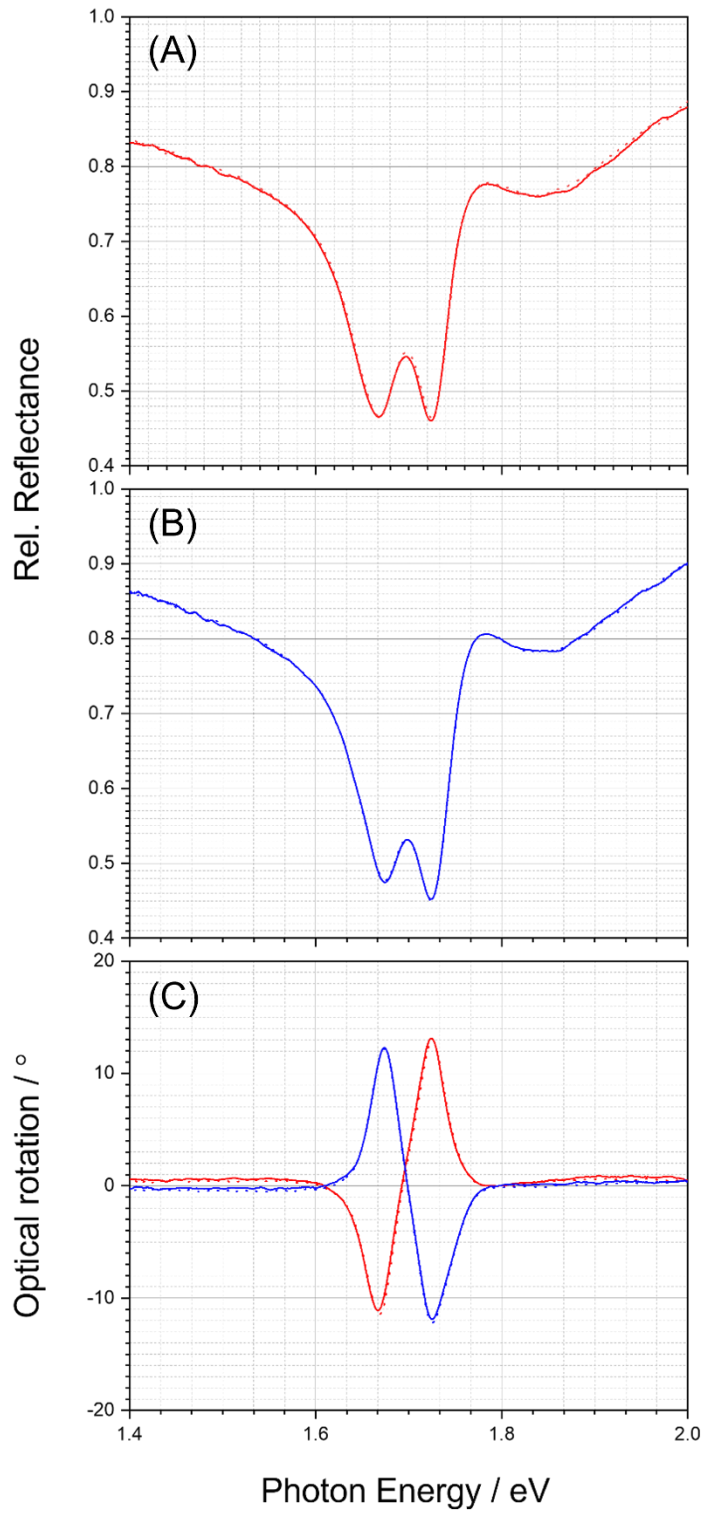


Figure 3. Reflectance spectra from (A) LH (red) and (B) RH (Blue) CQM. Spectra for un-complexed (solid) and complexed (dotted) CQMs. (C) Equivalent ORD spectra are shown. The data illustrated the negligible changes in spectra after complexation.

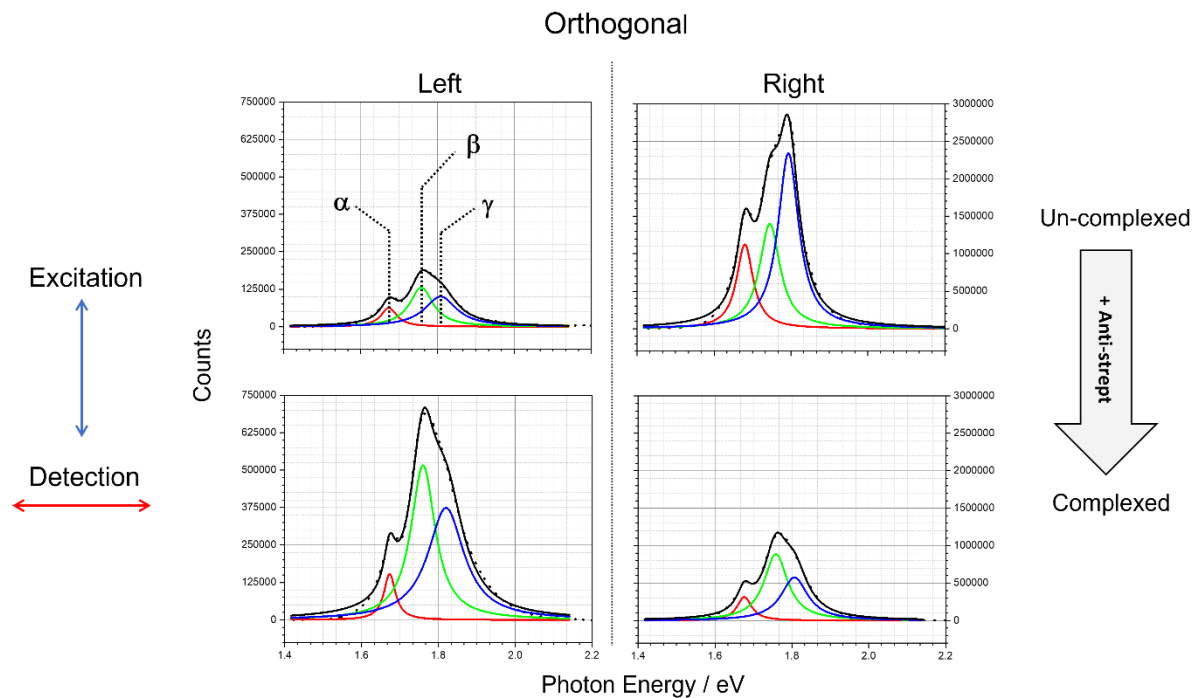


Figure 4. Luminescence spectra (dotted lines) collected using the orthogonal detection geometry from LH and RH enantiomorphs of un-complexed (upper panels) and complexed (lower panels) CQMs. Corresponding fits (solid lines) to three Lorentzians components, α (red) β (green) and γ (blue), are also shown.

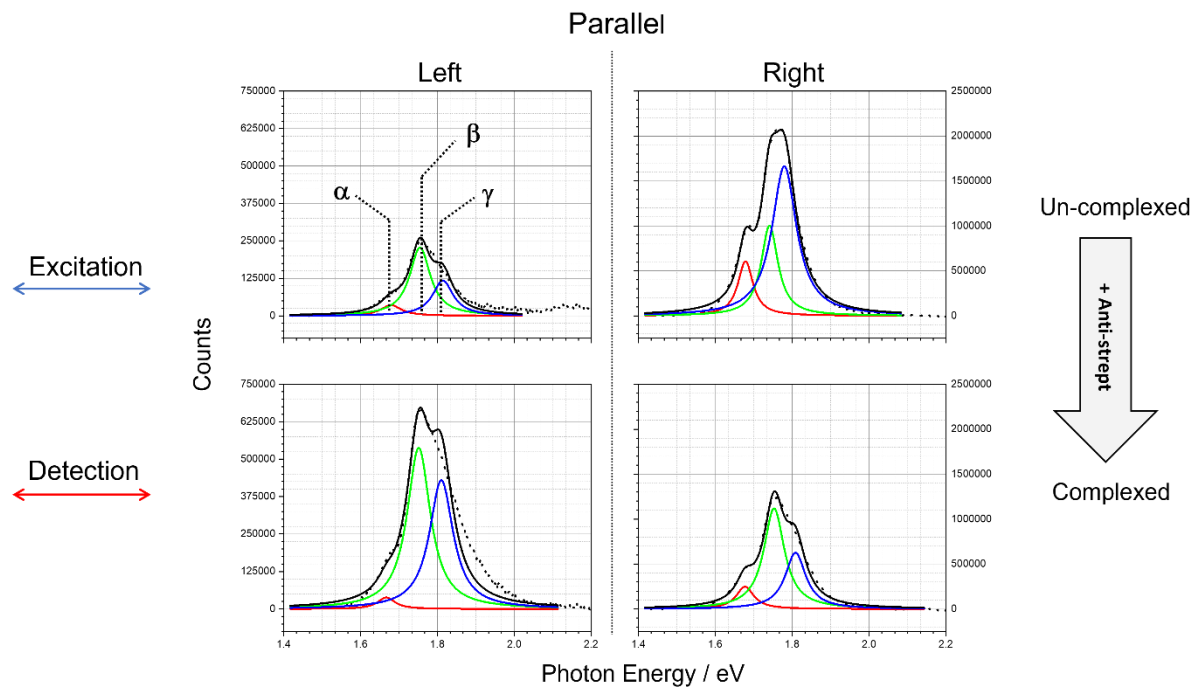


Figure 5. Luminescence spectra (dotted lines) collected using the parallel detection geometry from LH and RH enantiomorphs of un-complexed (upper panels) and complexed (lower panels) CQMs. Corresponding fits (solid lines) to three Lorentzians components, α (red) β (green) and γ (blue), are also shown.

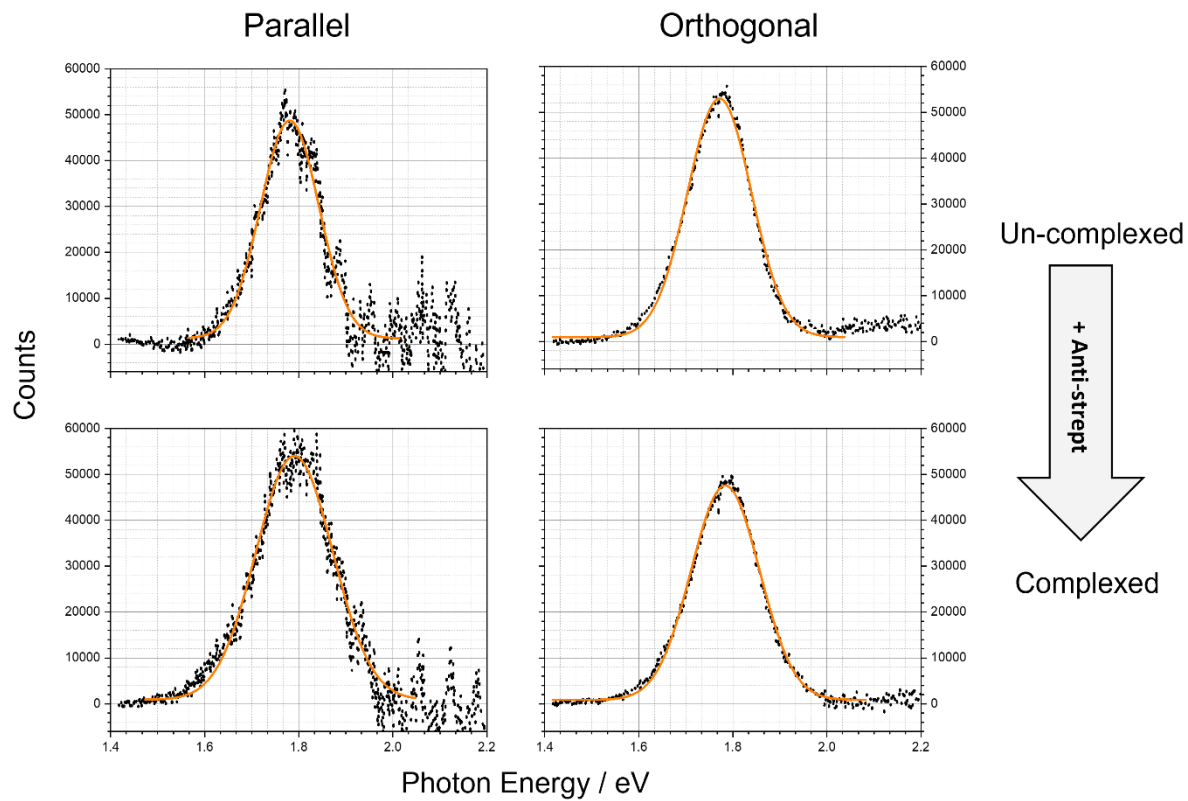


Figure 6. Luminescence spectra (dotted lines) collected using the parallel and orthogonal detection geometries from un-complexed (upper panels) and complexed (lower panels) QDs immobilised on an unstructured Au film. Corresponding fits (solid orange lines) using a single Gaussian component.

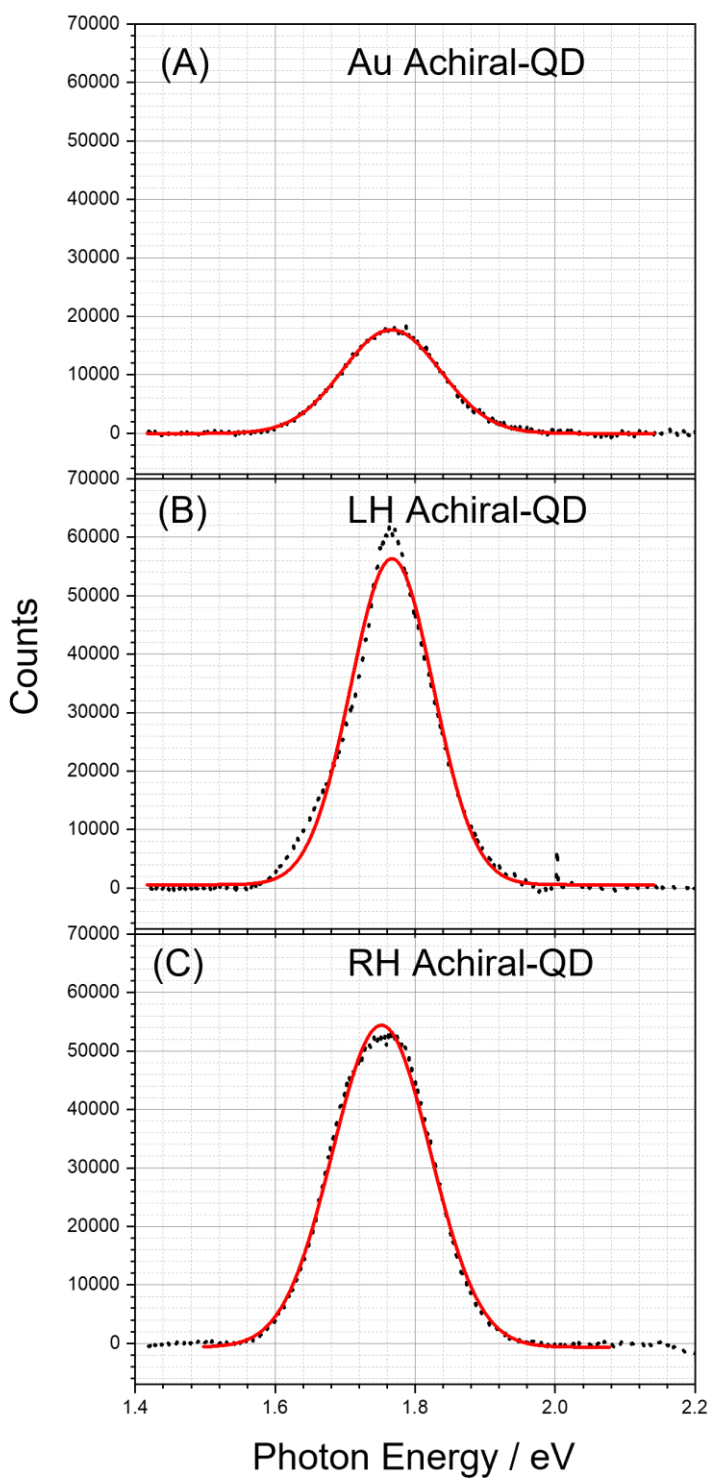


Figure 7. Luminescence spectra (dotted black line) collected in a parallel detection geometry from achiral QDs immobilised using EDC functionalisation strategy. Spectra are shown for QDs

immobilised on (A) unstructured Au, (B) LH and (C) RH shurikens. Each spectrum is fitted to a single Gaussian component.

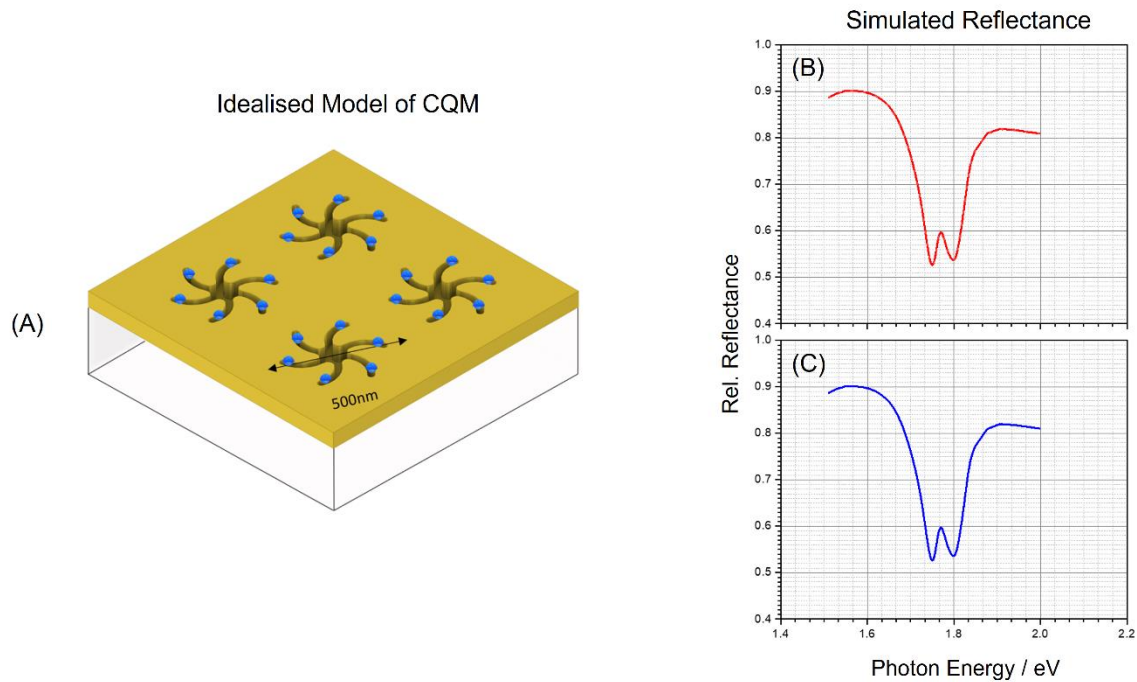


Figure 8. (A) A schematic of the idealised model of the CQM used in the numerical simulation is shown. Simulated spectra reflectance spectra for (B) LH and (C) RH un-complexed (dotted) and complexed CQMs are shown. For both LH and RH CQM the differences between the un-complexed and complexed spectra are undetectable above the line thickness.

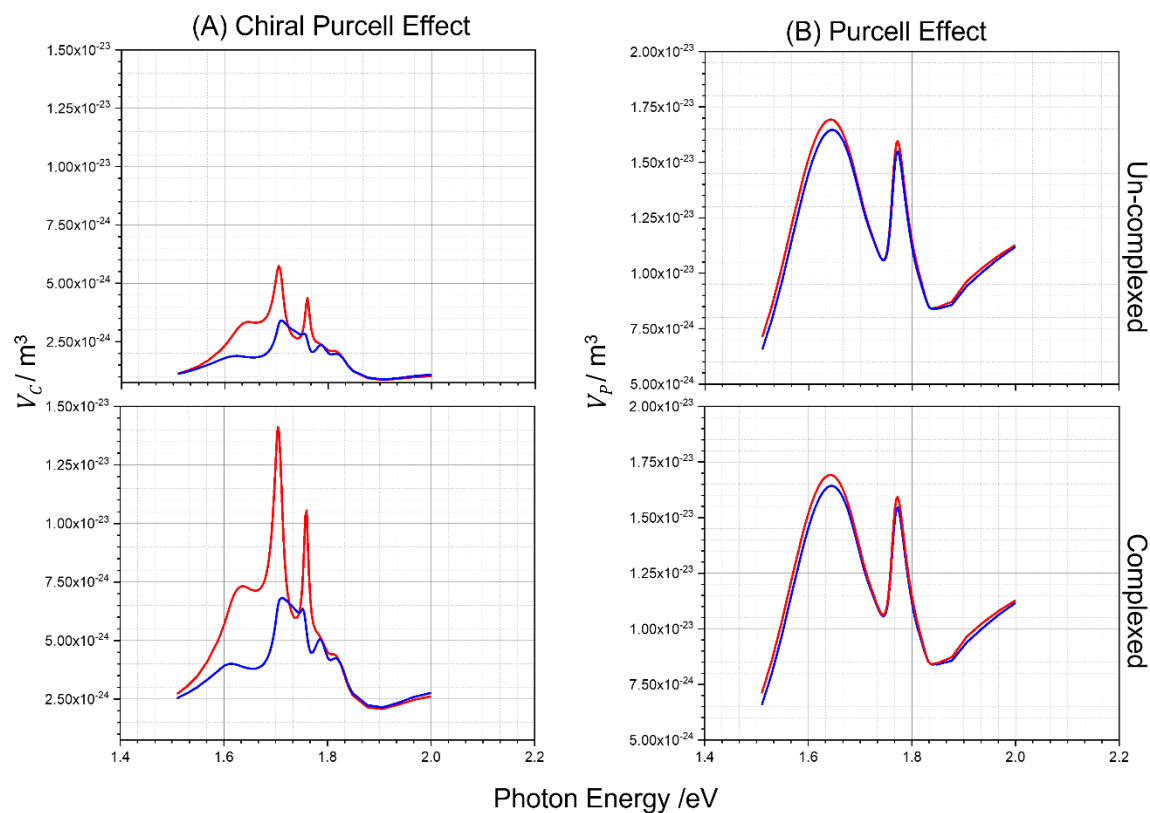


Figure 9. (A) Chiral mode volumes as a functions photon energy for un-complexed and complexed CQMS, for LH (red) and RH (Blue) enantiomorphs. (B) Equivalent data as in (A) but for the effective mode volume for the Purcell effect.

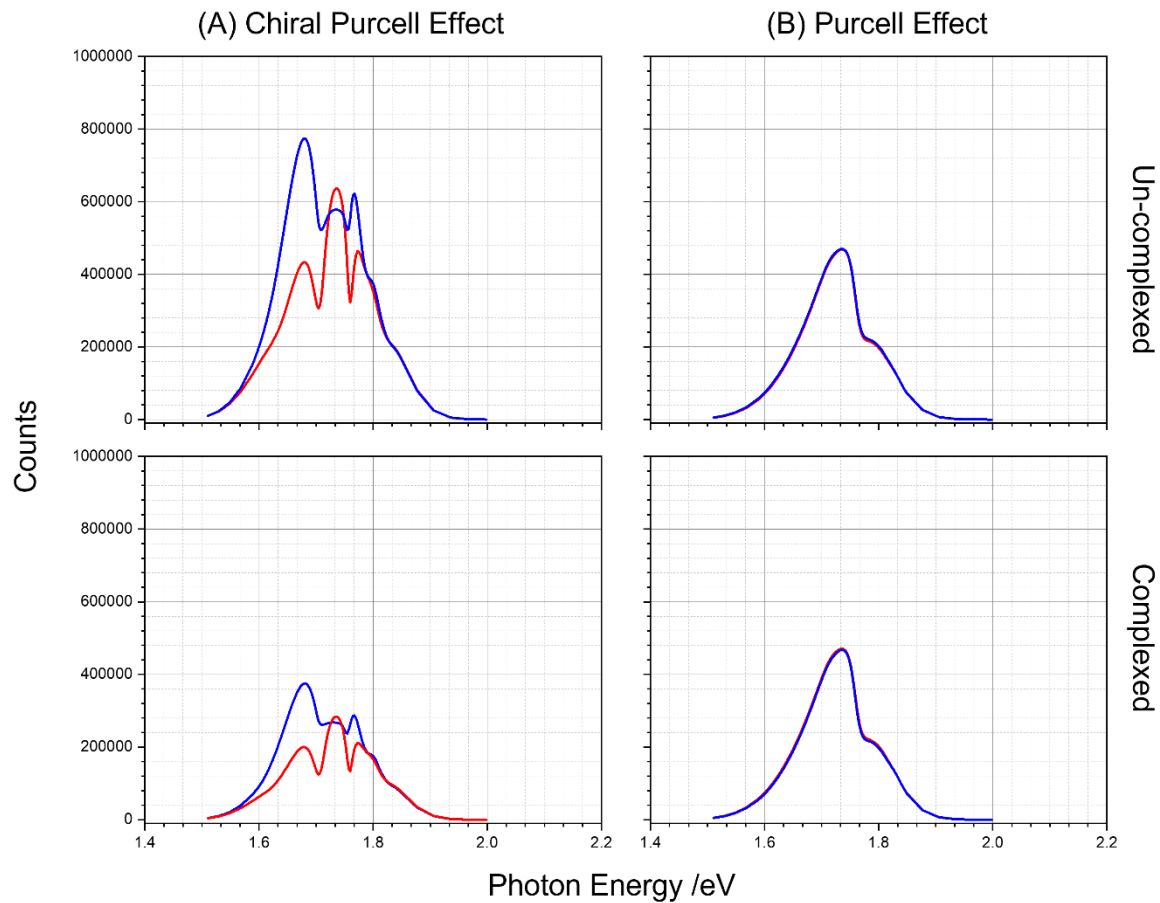


Figure 10. Simulated spectra (upper panels un-complexed, lower panels complexed) for LH (red) and RH (blue) enantiomorphs of CQMs derived from (A) V_C and (B) V_P . identical vertical scales have been used in all four panels.

		Depolarisation Ratio (ρ)
Un-complexed	LH	1.07±0.01
	RH	0.70±0.01
	Au	0.93±0.10
Complexed	LH	0.84±0.01
	RH	0.98±0.01
	Au	1.00±0.10
Achiral QD	LH	~0
	RH	~0
	Au	~0

Table 1. Values for the depolarisation (ρ) ratio for -un-complexed / complexed CQM and achiral reference are listed

	Asymmetry Factor (<i>A</i>)	
	Orthogonal	Parallel
Un-complexed	13.0±0.1	8.5±0.1
Complexed	1.5±0.1	1.7±0.1
Achiral QD		1.2±0.4

Table 2. Values for the asymmetry factor (*A*) ratio for -un-complexed / complexed CQM and achiral reference are listed

		Enhancement Factor (F)	
		Orthogonal	Parallel
Un-complexed	LH	4.2±0.1	4.7±0.1
	RH	54.4±0.5	40.4±0.5
Complexed	LH	15.6±0.2	11.9±0.2
	RH	23.0±0.2	20.5±0.2
Achiral QD	LH		2.7±0.4
	RH		3.1±0.4

Table 3. Values for the asymmetry factor (F) ratio for -un-complexed / complexed CQM and achiral reference are listed